Scalable, durable, and safe enough for the power grid.

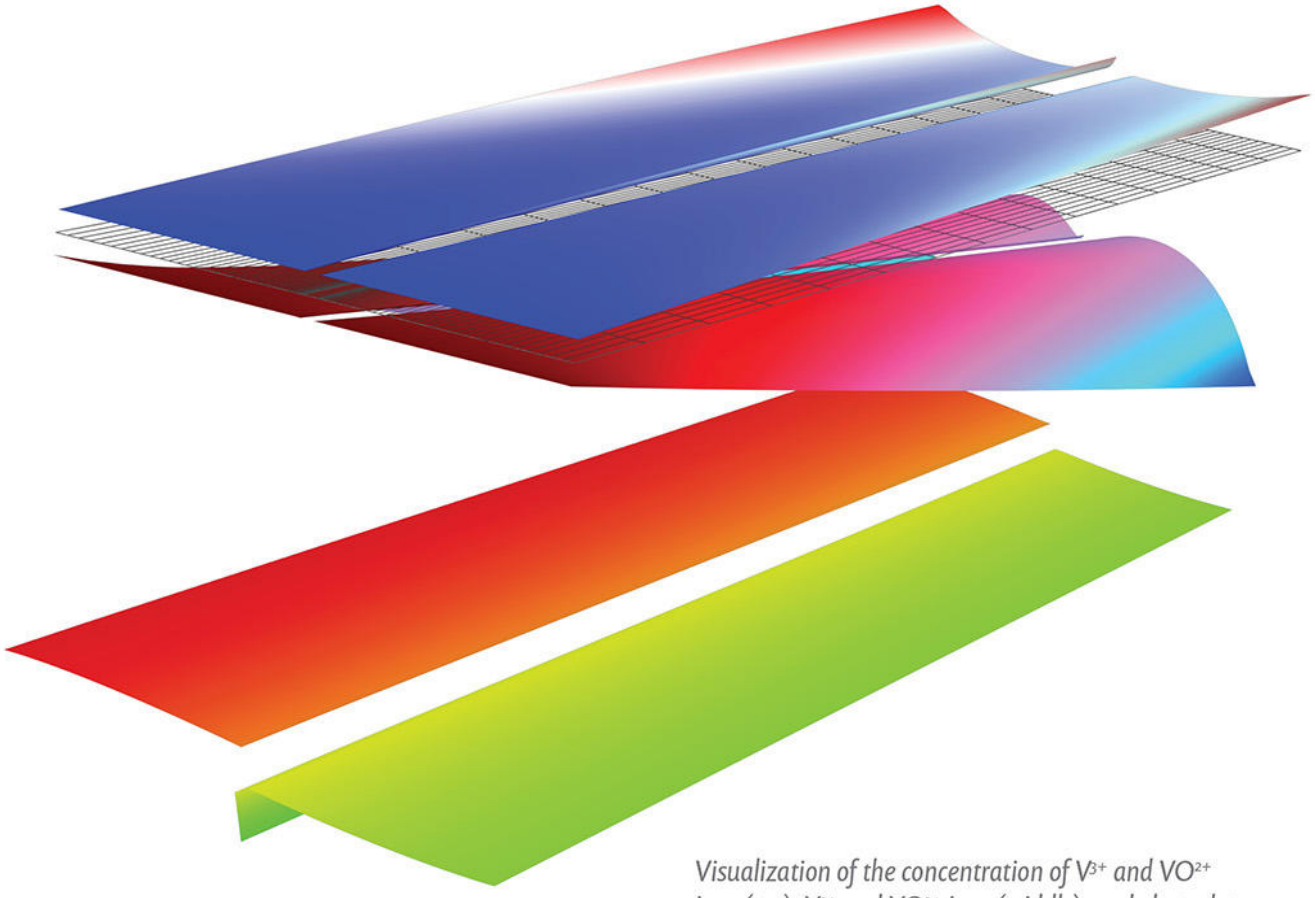

Visualization of the concentration of V^{3+} and VO^{2+} ions (top), V^{2+} and VO^{2+} ions (middle), and electrolyte potential (bottom) in a vanadium redox flow battery.

When developing rechargeable batteries for the power grid, vanadium is a stronger contender than lithium. Advantages include scalability, longer and more consistent operation lifetimes, safety, and the ability to fill in the gaps when wind or solar power suffers intermittency issues. But vanadium redox flow batteries (VRFBs) do bring shortcomings of their own. Engineers looking to improve grid energy storage and reliability often start by optimizing VRFB designs.

The COMSOL Multiphysics® software is used for simulating designs, devices, and processes in all fields of engineering, manufacturing, and scientific research. See how you can apply it to modeling vanadium redox flow batteries.

comsol.blog/VRFB

COMSOL

ADVANCED ENERGY MATERIALS

www.advenergymat.de

Ultrathin High Surface Area Nickel Boride (Ni_xB) Nanosheets as Highly Efficient Electrocatalyst for Oxygen Evolution

Justus Masa, Ilya Sinev, Hemma Mistry, Edgar Ventosa, Maria de la Mata, Jordi Arbiol, Martin Muhler, Beatriz Roldan Cuenya, and Wolfgang Schuhmann**

The overriding obstacle to mass production of hydrogen from water as the premium fuel for powering our planet is the frustratingly slow kinetics of the oxygen evolution reaction (OER). Additionally, inadequate understanding of the key barriers of the OER is a hindrance to insightful design of advanced OER catalysts. This study presents ultrathin amorphous high-surface area nickel boride (Ni_xB) nanosheets as a low-cost, very efficient and stable catalyst for the OER for electrochemical water splitting. The catalyst affords 10 mA cm^{-2} at 0.38 V overpotential during OER in 1.0 M KOH, reducing to only 0.28 V at 20 mA cm^{-2} when supported on nickel foam, which ranks it among the best reported nonprecious catalysts for oxygen evolution. Operando X-ray absorption fine-structure spectroscopy measurements reveal prevalence of NiOOH, as well as Ni-B under OER conditions, owing to a Ni-B core@nickel oxyhydroxide shell (Ni-B@NiO_xH) structure, and increase in disorder of the NiO_xH layer, thus revealing important insight into the transient states of the catalyst during oxygen evolution.

1. Introduction

Electrochemical water splitting for hydrogen production is impeded by intensive energy consumption mostly due to the slow kinetics of the oxygen evolution reaction (OER), and the requirement to use costly and rare platinum group metal (PGM) catalysts, rendering the process of low economic appeal.[1] Efforts to reduce or completely substitute the use of PGM electrocatalysts (Pt, IrO_2, and RuO_2), the state-of-the catalysts for electrochemical water splitting (ECWS), with less costly alternatives to leverage the competitiveness of ECWS have been futile in the past.[2] Moreover, even with Pt as the cathode, and RuO_2 or IrO_2 as the anode, large overpotentials are still incurred to achieve meaningful electrolysis rates.[3] ECWS using nonprecious metal catalysts is more promising in high pH electrolytes, where Ni, Co, and Fe-based materials are very promising.[4] Specifically, mixed metal oxides and hydroxides,[5–7] and compounds of Co and Ni incorporating nonmetal elements, typically, B, N, S, Se, and P,[8–10] have proved phenomenal in alkaline water oxidation, with activities surpassing RuO_2 and IrO_2 being reported for NiSe, Ni_5P_4, Ni_2P, CoP, and Ni_3N, among others. Meanwhile, binary and ternary compounds of Co, Fe, Mo, W, and Ni with B, P, S, and Se, among others also exhibit outstanding activity in catalyzing the hydrogen evolution reaction.[9,11] These developments inspire new directions in the search for advanced nonprecious catalysts for ECWS. For electrochemical applications, high surface area materials either with a layered structure or high porosity,[11,12] but most preferably those which combine both of these properties, are desirable owing to their high active site densities, which favor a high active site utilization.

Herein, we report the synthesis of ultrathin high surface area amorphous nickel boride (Ni_xB) nanosheets and demonstrate their remarkable activity and stability as nonprecious metal catalyst for oxygen evolution under alkaline conditions. The catalyst afforded 10 mA cm^{-2} at 0.38 V overpotential during OER in 1.0 M KOH, which reduced to only 0.28 V at 20 mA cm^{-2} when supported on nickel foam. Additionally, we present insight from operando X-ray absorption fine-structure spectroscopy (XAFS) of the nature of transient states of the

Dr. J. Masa, Dr. E. Ventosa, Prof. W. Schuhmann
Analytical Chemistry—Center for Electrochemical Sciences (CES)
Ruhr Universität Bochum
D-44780 Bochum, Germany
E-mail: justus.masa@rub.de; wolfgang.schuhmann@rub.de
Dr. I. Sinev, Dr. H. Mistry, Prof. B. Roldan Cuenya
Department of Physics
Ruhr-University Bochum
D-44801 Bochum, Germany
Dr. H. Mistry
Department of Physics
University of Central Florida
Orlando, FL 32816, USA
M. de la Mata, Prof. J. Arbiol
Catalan Institute of Nanoscience and Nanotechnology (ICN2)
CSIC, and The Barcelona Institute of Science and Technology (BIST)
Campus UAB, Bellaterra, 08193 Barcelona, Catalonia, Spain
Prof. J. Arbiol
ICREA
Pg. Lluís Companys 23, 08010 Barcelona, Catalonia, Spain
Prof. M. Muhler
Laboratory of Industrial Chemistry
Ruhr-University Bochum
D-44801 Bochum, Germany
The ORCID identification number(s) for the author(s) of this article can be found under https://doi.org/10.1002/aenm.201700381.

DOI: 10.1002/aenm.201700381

catalyst during oxygen evolution. The active form of the catalyst is a Ni-B@NiOOH (core@shell) structure. We observed a contraction of the Ni—O bonds in NiOOH accompanied with increase in disorder of the layer, and very fast deoxygenation of the terminal intermediate during active oxygen evolution.

2. Results and Discussion

Nickel boride (Ni_xB) was prepared by chemical reduction of nickel ions in a deaerated 1.0 M $NiCl_2*6H_2O_{(aq)}$ solution using 1.0 M $NaBH_{4(aq)}$ in 0.1 M NaOH (see the Supporting Information for details). The composition of Ni and B in the product was 76.2% and 6.6%, respectively, corresponding to a Ni:B stoichiometry of 2:1 (Table S1, Supporting Information), the rest being mostly oxygen (Figure S1, Supporting Information). X-ray diffraction (XRD) studies **(Figure 1)** revealed Ni_xB to be XRD amorphous. The product remained XRD amorphous upon annealing under Ar at 300 °C for 2 h. Further increase of the annealing temperature to 600 °C led to crystallization and emergence of Ni_3B (ICSD: 614985) as the major phase, and Ni_2B (ICSD 75792) as a minor phase. Ni_3B remained the dominant phase in the sample annealed at 1000 °C, with minor reflections assignable to Ni_2B also detectable. Structure refinement using Rietveld analysis revealed that Ni_xB-1000 contained 79% Ni_3B while Ni_2B made up 21%. Ni_xB annealed at 300 °C (Ni_xB-300) exhibited the best electrochemical performance (discussed later) and was thus characterized in more detail.

Ni_xB-300 is comprised of very thin sheets as well as discrete particles (Figure 1b). High-resolution transmission electron microscopy (HRTEM) analysis of an individual flake of Ni_xB-300 (Figure 1c) reveals atomically thin layers with a thickness of about 6.6 Å (Figure 1d).

Atomic force microscopy (AFM) images of Ni_xB-300 recorded in the tapping mode and the corresponding height profile (Figure S3, Supporting Information) revealed that the individual nanosheets were predominantly about 1.0 nm thick, with lateral dimensions being in the range of ≈200–300 nm.

Spectroscopic analysis by electron energy loss spectroscopy shows that the discrete particles are predominantly nickel boride, while the sheets have a uniform distribution of Ni, B, as well as oxygen (Figure S3, Supporting Information). Fast

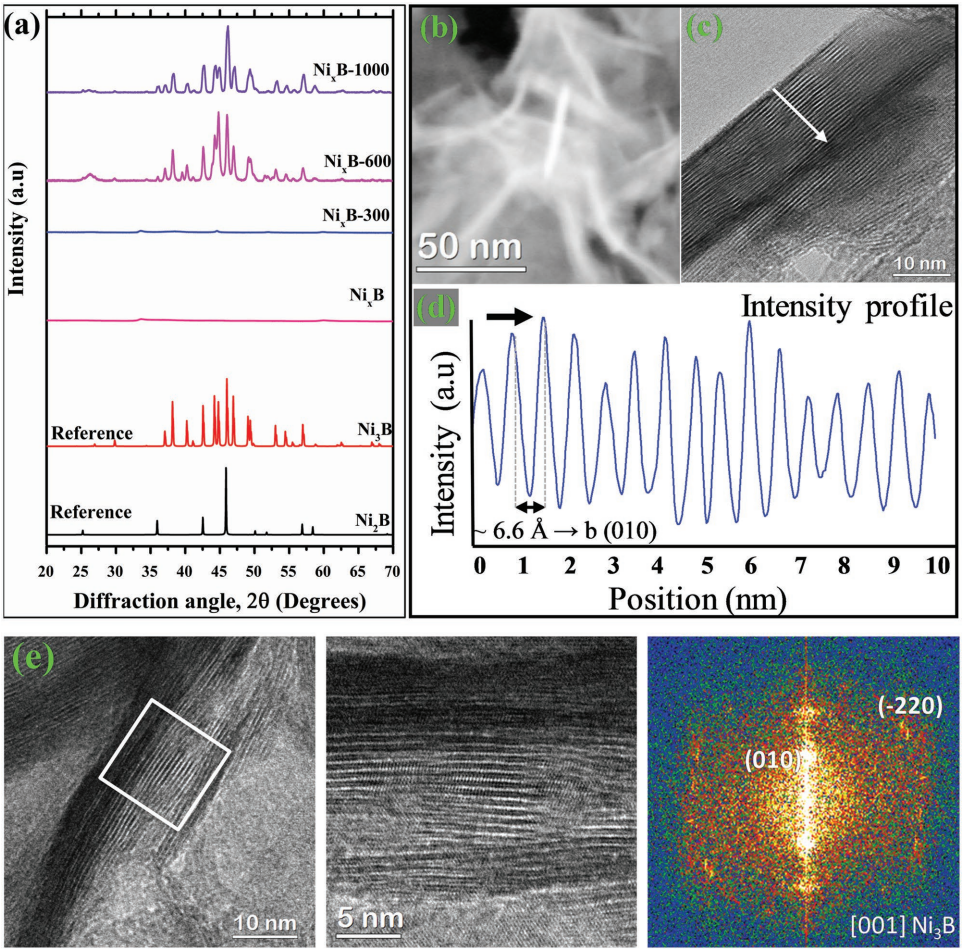

Figure 1. a) XRD patterns of Ni_xB, Ni_xB annealed at 300 °C (Ni_xB-300), 600 °C (Ni_xB-600), and at 1000 °C (Ni_xB-1000), and of the references Ni_2B (ICSD 75792) and Ni_3B (ICSD 614985). b) High-angle annular dark field (HAADF) low magnification TEM micrograph of Ni_xB-300, c) HRTEM of a single flake showing layers of sheets, d) intensity profile taken across the flake along the white arrow in (c) showing individual sheets with a thickness of ≈6.6 Å. e) HRTEM image of Ni_xB-300 with a magnified view of the rectangular marked region and its corresponding FFT pattern.

Fourier transform (FFT) analysis of selected regions of the HRTEM images disclosed predominance of Ni_2B nanocrystallites in Ni_xB-300 (Figure S4, Supporting Information). Crystallites of Ni_3B were also occasionally found (Figure 1e). In consideration of the XRD and TEM observations, it can be concluded that Ni_xB-300 was composed of nanocrystallites of Ni_2B, and Ni_3B to a less extent, as well as very small particles of $Ni^{(0)}$. The predominance of the Ni_3B phase at high annealing temperatures, as confirmed by XRD, indicates thermally induced transition of Ni_2B to Ni_3B, and also suggests the reaction of Ni with Ni_2B to form Ni_3B ($Ni + Ni_2B \rightarrow Ni_3B$), consistent with the work of Glavee et al. [13], among others.

X-ray photoelectron spectroscopy (XPS) examination of the chemical state of as prepared Ni_xB minimally exposed to air showed the main Ni $2p_{3/2}$ and Ni $2p_{1/2}$ core peaks at 852.5 and 869.6 eV (**Figure 2**a(i)), respectively, typical of Ni_2B.[14] The Ni $2p_{3/2}$ and Ni $2p_{1/2}$ satellite peaks at 855.6 and 873.0 eV, respectively, are due to Ni^{2+}, indicating the presence of surface oxide or hydroxide species. Amorphous metal borides are spontaneously oxidized when exposed to air and water to form surface oxides/hydroxides leading to a core@shell (metal boride@metal oxide/hydroxide) structure.[15] Ni_xB exposed to air, (Figure 2a(ii)), thus exhibited a predominantly oxidized surface with a dominant Ni $2p_{3/2}$ peak at 855.82 eV (Ni^{2+} species) and minor peak at 852.52 eV due to the interaction of nickel with boron (Figure 2a).

A positive chemical shift of 0.95 eV in the binding energy of the Ni $2p_{3/2}$ peak was observed upon annealing Ni_xB at 300 °C (Figure 2c), indicating relative displacement of electrons from nickel. The annealing process thus led to modification of the surface electronic structure of Ni_xB-300, which had a beneficial effect on its OER activity.

The B 1s spectrum of as prepared Ni_xB minimally exposed to air (Ni_xB-(i) in Figure 2b) was deconvoluted into two distinct species at 187.9 and 191.8 eV (Figure 2b). The species at 187.9 eV is due to interaction of boron with nickel, whereas the one at 191.8 eV is due to boron-oxo species. On the other hand, the B 1s spectrum of Ni_xB exposed to air for several hours (Ni_xB-(ii) in Figure 2b) was deconvoluted into two contributions at 190.07 and 192.0 eV both corresponding to boron oxide species.

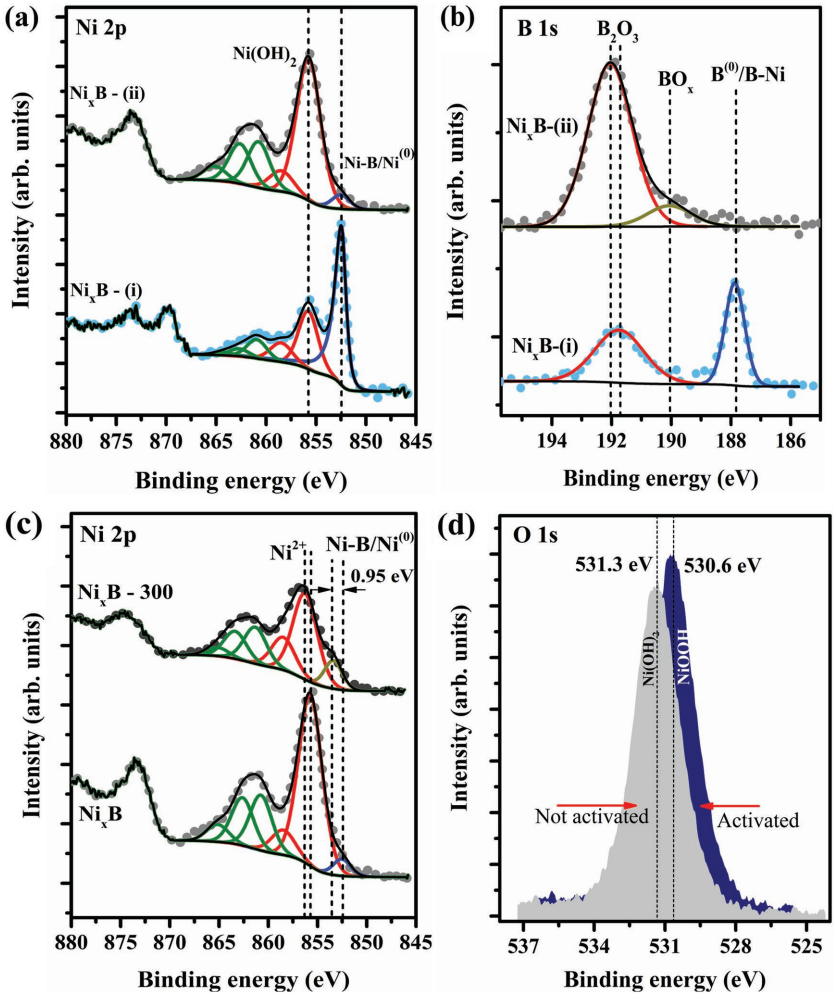

Figure 2. XPS analysis: a) Ni 2p and b) B 1s core-level spectra of Ni_xB minimally exposed to air (i) and after prolonged air exposure (ii). c) Ni 2p core-level spectra of Ni_xB and Ni_xB after annealing under argon at 300 °C, and d) O 1s high-resolution spectra of Ni_xB-300 before and after electrochemical activation.

The O 1s spectrum of Ni_xB-300 (Figure 2d), not activated sample, shows that its surface was covered with $Ni(OH)_2$. Meanwhile, after electrochemical activation (activated in Figure 2d), which involved 50 cycles of potential cycling in 1.0 M KOH between 0.95 and 1.65 V versus RHE (Reversible hydrogen electrode), the surface was mainly covered with a nickel oxyhydroxide (NiOOH) layer.

XAFS measurements were carried out on Ni_xB, Ni_xB-300, and Ni_xB-1000 to probe the influence of annealing temperature on the chemical state and local coordination structure of the catalyst. X-ray absorption near edge structure (XANES) spectra are presented in **Figure 3**a. The pre-edge region of Ni_xB and Ni_xB-300 consist of a small peak at ≈8333 eV whose shape and position match very well with $Ni(OH)_2$ and NiO (not shown) reference spectra. The first feature above the absorption edge (white-line) centered at 8351 eV is also in agreement with the NiO and $Ni(OH)_2$ spectra, thus indicating predominance of the Ni^{2+} state in the samples. On the other hand, the XANES spectrum of Ni_xB-1000 shows close resemblance to a commercial nickel boride reference (Sigma-Aldrich), featured by a white line significantly less intense than the Ni^{2+} references. In this case, the XANES results are in good agreement with XRD data described before. However, the reference nickel boride sample, NiB (Sigma-Aldrich), was composed of several distinct Ni_xB_y phases and was thus not a suitable reference for discussion of the extended X-ray absorption fine-structure (EXAFS) data following hereafter.

EXAFS spectra of Ni_xB, Ni_xB-300, and Ni_xB-1000 (Figure 3b) reveal significant

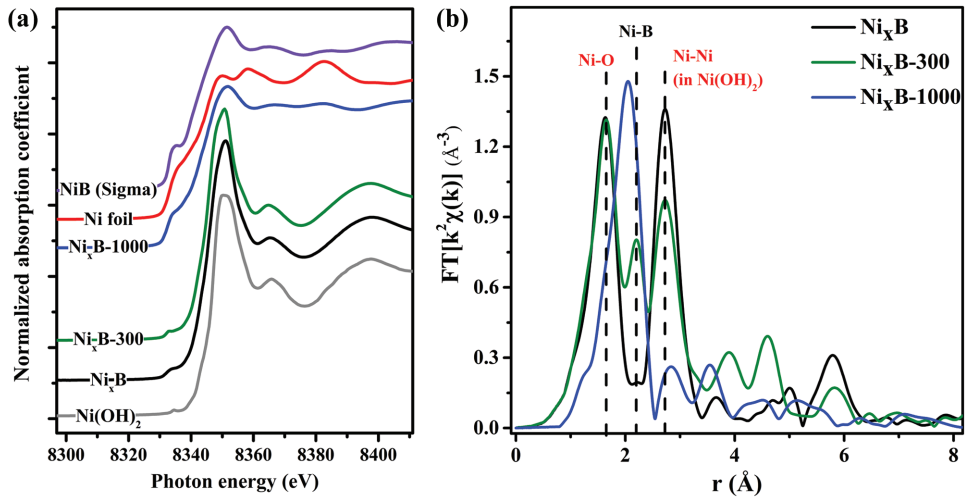

Figure 3. a) X-ray absorption near-edge structure (XANES) spectra of the as prepared Ni_xB sample, Ni_xB annealed at 300 °C (Ni_xB-300) under argon, Ni_xB annealed at 1000 °C under argon (Ni_xB-1000), a Ni-foil, NiB (Sigma-Aldrich) and $Ni(OH)_2$ as references. b) Extended X-ray absorption fine structure (EXAFS) spectra of Ni_xB, Ni_xB-300, and Ni_xB-1000.

differences induced by the annealing processes on the local environment of nickel. The shapes of both Ni_xB and Ni_xB-300 spectra show the presence of backscattering events characteristic of Ni^{2+} compounds, namely, Ni-O at 2.07 Å and Ni-Ni at 3.1 Å (uncorrected for phase shift). There is an extra peak emerging at 2.2 Å (uncorrected) on the EXAFS spectrum of the sample annealed at 300 °C indicating the presence of B in a local Ni environment. Moreover, peak separation of the spectrum for the untreated Ni_xB sample with a plateau between 2.1 and 2.3 Å gives hint of a similar Ni-B coordination. Detailed analysis of the EXAFS spectra performed by fitting a combination of Ni-O, Ni-B, and Ni-Ni^{2+} backscattering paths to the spectral features described above gives proof to the hypothesis of the presence of boron as nearest neighbor in Ni local coordination (see Table S2 of the Supporting Information for details). Thus, in the as prepared Ni_xB sample, the effective Ni-B coordination number is as low as 1.8, while a high value of the corresponding σ^2 (11.9×10^{-3} Å^2) indicates significant disorder in the boride structure. Annealing at 300 °C results in an increase of the Ni-B coordination number to 4.2, and ordering of the boride structure with a less ordered $Ni(OH)_2$ phase evidenced by a lower Ni-Ni^{2+} coordination number and higher σ^2. The EXAFS spectrum of Ni_xB-1000 is dominated by a peak at 2.05 Å (uncorrected), and can be fitted for the most by Ni-B and a minor amount of Ni-O. The Ni-B coordination number as high as 13.4 in this case can be interpreted by overlapping of several Ni-B backscattering events from different well-ordered Ni_xB_y phases, as indicated by XRD.

A film of Ni_xB was adsorbed on a glassy carbon electrode and investigated for electrocatalysis of OER in 1.0 M KOH (see the Supporting Information for details of film preparation). Before acquiring any electrochemical data, the electrode was first subjected to continuous potential cycling at a scan rate of 0.1 V s^{-1} between 0.95 and 1.65 V (RHE) until reproducible voltammograms were obtained (**Figure 4**a). The continuous increase in the intensity of both the anodic and cathodic peaks centered at about 1.40 V is due to growth of a NiOOH layer (Figure 2d). The anodic process is due to oxidation of Ni^{2+} to Ni^{3+}, while the reverse process is the reduction of Ni^{3+} back to Ni^{2+}, that is, $Ni(OH)_2 + OH^- \leftrightarrow NiOOH + H_2O + e$. Results for electrocatalysis of the OER by Ni_xB in 1.0 M KOH are presented in Figure 4b. The OER activity of Ni_xB became enhanced upon annealing in argon for 2 h, reaching a maximum at 300 °C followed by a drastic decline at higher annealing temperatures. The catalyst was not able to attain 10 mA cm^{-2} within the investigated potential window (1.0–1.8 V) when annealed at or above 700 °C. The inset of Figure 4b shows variation of the OER activity of Ni_xB with annealing temperature, expressed as the potential corresponding to a current density of 10 mA cm^{-2}. The nonannealed sample, Ni_xB, attained 10 mA cm^{-2} at 1.73 V, while Ni_xB-200 and Ni_xB-300 afforded 1.68 and 1.61 V, respectively, at the same current density. Importantly, Ni_xB-300 exhibited better OER activity than Ni_xB-200 despite the former possessing a slightly lower Brunauer-Emmett-Teller (BET) surface area, 122.3 m^2 g^{-1} for Ni_xB-300 versus 127.4 m^2 g^{-1} for Ni_xB-200 (Table S1, Supporting Information). This implies that increase of the OER activity from Ni_xB through Ni_xB-200 and Ni_xB-300 cannot be explained in terms of surface area.

It is worth to note that the intensity of the $Ni^{2+} \leftrightarrow Ni^{3+}$ redox peaks followed a trend exactly similar to the OER activity dependence on temperature. Characteristically, the area under the $Ni^{2+} \leftrightarrow Ni^{3+}$ redox peaks is proportional to the amount of electrochemically addressable nickel atoms/ions, which is intimately linked to conductivity. The observed enhancement of the OER activity with annealing temperature is thus mainly attributed to increase of the electrical conductivity of the catalyst due to sintering of the catalyst particles. Besides affecting the geometrical properties, XPS analysis revealed that the annealing process also induces changes in the chemical state of the catalyst surface ascribed to electronic structure modification. For example, a positive chemical shift in the binding energy (BE) of the Ni 2p3/2 peak of 0.95 eV, from 852.4 eV to 853.5 eV, was observed when Ni_xB was annealed at 300 °C (Figure 2c). The decline in activity at much higher annealing

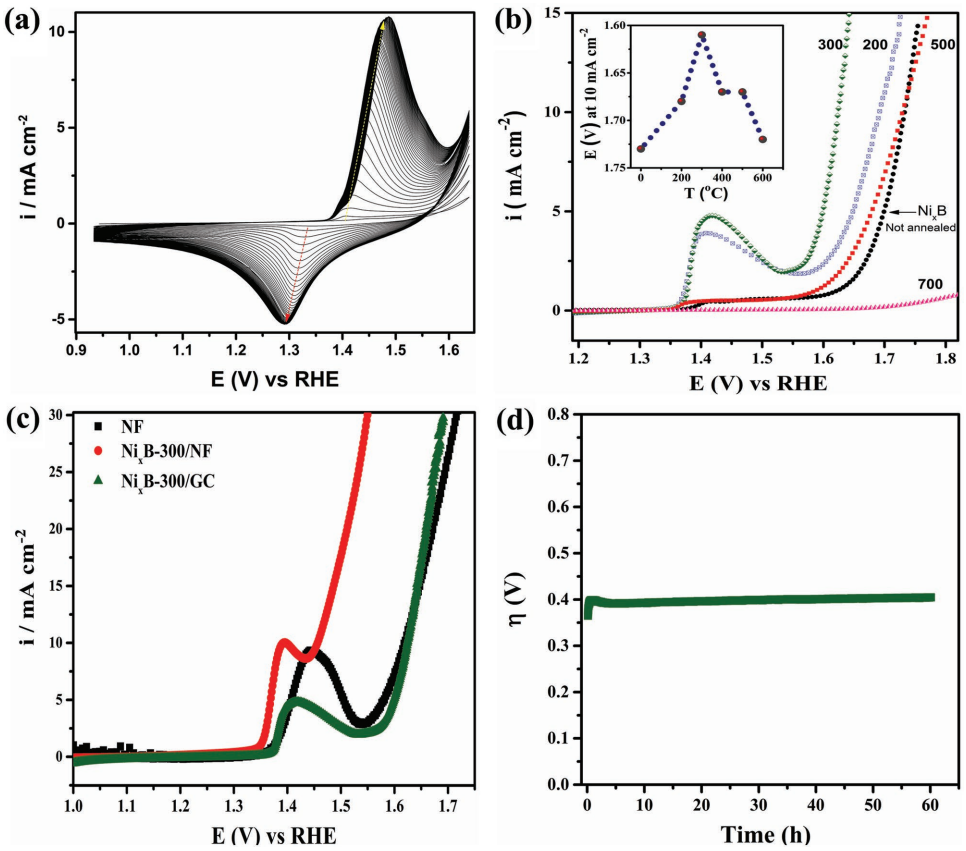

Figure 4. a) Activation of Ni_xB by continuous potential cycling between 0.95 and 1.65 V at 100 mV s^{-1} in 1.0 M KOH; b) Linear sweep voltammograms (LSVs), corrected for the resistance of the electrolyte, of Ni_xB and Ni_xB annealed at 200, 300, 500, and 700 °C, recorded at 10 mV s^{-1} in 1.0 M KOH and at 1600 rpm electrode rotation. Inset: Variation of the OER activity of Ni_xB, expressed as the potential at a current density of 10 mA cm^{-2}, with annealing temperature. c) Comparative LSVs of a bare nickel foam (NF) electrode, and Ni_xB-300 supported on glassy carbon (Ni_xB-300/GC) and on nickel foam (Ni_xB@NF) in 1.0 M KOH; c) Galvanostatic long-term stability measurement of Ni_xB-300 deposited on a graphite rotating disk electrode (area = 0.196 cm^2) at 10 mA cm^{-2} in KOH (1.0 M).

temperatures is certainly due to decrease of the surface area due to the growth in particle size. The BET surface area decreased from 122.3 m^2 g^{-1} (Ni_x B-300) to 16.3 m^2 g^{-1} for Ni_xB-600, and 7.9 m^2 g^{-1} for Ni_xB-1000.

Galvanostatic stability measurements of Ni_xB-300 supported on a graphite ring-disk electrode (RDE) at a current density of 10 mA cm^{-2} in 1.0 M KOH indicate very stable performance of the catalyst with essentially no loss in performance after 60 h (Figure 4d). The Faraday efficiency, determined using the rotating ring-disk electrode technique,[16] was 98.9% (Figure S11, Supporting Information), indicating that the applied current was nearly exclusively used for oxygen evolution. In metal borides, the boron atoms are capable of forming linear, planar, and 3D structures surrounded by metals,[17] through the formation of covalent M-B, as well as B—B bonds, making these compounds extremely hard and chemically resistant.

Nickel foam (NF) is an attractive 3D catalyst support for gas evolution electrodes owing to its high surface area, stability, and synergistic catalytic effect.[6,18,19] We supported Ni_xB-300 on nickel foam (Ni_xB-300/NF) and investigated the resulting electrodes for the OER in a custom-built flow-through cell.[20] **Figure 5**a shows the OER performance of the Ni_xB-300/NF electrode in 1.0 M KOH compared to Ni_xB-300 supported on glassy carbon (Ni_xB-300/GC), and bare NF. Employing NF as a support led to tremendous increase of the current and significant reduction of the overpotential. In our case, it was not valid anymore to extract the potential corresponding to a current density of 10 mA cm^{-2} since this overlapped with the gigantic $Ni^{2+} \rightarrow Ni^{3+} + e^-$ oxidation wave. A current density of 20 mA cm^{-2} (normalized to geometric electrode area) was attained at an overpotential of only 0.28 V. To benchmark the performance of Ni_xB-300, its activity was compared against some recently reported highly active nonprecious OER catalysts, particularly, nickel-based catalysts supported on nickel foam (Table S3, Supporting Information). As an example, a NiFe double layer hydroxide doped with nitrogen (N-NiFe-LDH) directly grown on nickel foam afforded 0.23 V overpotential at a current density of 10 mA cm^{-2} in 1.0 M KOH.[21] A NiCoP catalyst supported on nickel foam delivered a current of 10 mA cm^{-2} at an overpotential of 0.28 V in 1.0 M KOH.[22] A gelled material comprised of a ternary homogeneous mixture of Fe, Co, and W oxyhydroxides delivered a current density of 10 mA cm^{-2} at an overpotential of 0.19 V during OER in 1.0 M KOH.[23] A recently reported cobalt phosphide Co/Co_2P oxygen evolution catalyst supported on nickel foam afforded 50 mA cm^{-2} at only 0.19 V

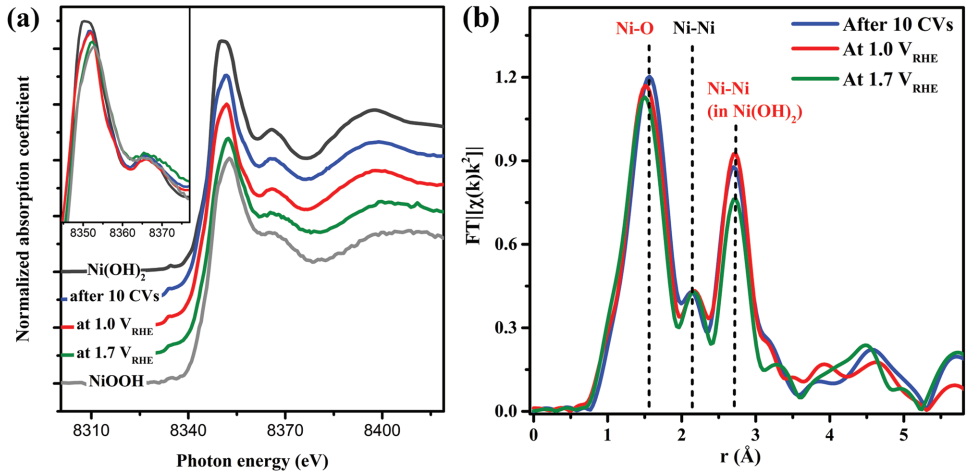

Figure 5. a) Operando XANES and b) EXAFS spectra of Ni_xB-300 acquired after conditioning (10 CVs) during OER at different electrochemical potentials, 1.0 and 1.7 V versus RHE.

overpotential.[24] The performance of Ni_xB-300 is thus clearly very promising and among the best reported for nickel-based catalysts. Importantly, Ni_xB-300 required the same potential (0.38 V) to deliver 10 mA cm^{-2} as RuO_2 and IrO_2 (Figure S12, Supporting Information). The Tafel slope of Ni_xB-300 $\left(\frac{\partial E}{\partial(\ln i)}\right)$, derived from Figure 4b, was 89 mV dec^{-1}, while that for OER on RuO_2 was 88 mV dec^{-1} and 90 mV dec^{-1} on IrO_2. The Tafel slopes of the OER are essentially similar and suggest that the rate limiting step on these catalysts is a coupled chemical-charge transfer step.[25] The turnover frequency (TOF) of oxygen evolution, calculated with respect to the total estimated amount of Ni in the catalyst (Ni = 79.1%, inductively coupled plama - mass spectrometry (ICP-MS) data), at 1.60 V (0.37 V overpotential), was ≈0.048 s^{-1} on Ni_xB-300, whereas it was ≈0.098 s^{-1} on RuO_2. Therefore, since the TOF is an intensive catalytic parameter, the results show that RuO_2 was potently more active than Ni_xB-300 on a per active site basis despite the catalysts exhibiting a similar overpotential at 10 mA cm^{-2}. Ni_xB-300 thus evidently benefitted from its high surface area, 122 m^2 g^{-1} compared to 1.2 m^2 g^{-1} for RuO_2, which facilitated a higher catalyst utilization.

The chemical state and structure of the catalyst under OER conditions was probed via operando XAFS studies. Figure 5 presents overlaid operando XANES (a) and EXAFS (b) spectra of Ni_xB-300 after electrochemical conditioning between 1.0 and 1.6 V, during polarization at 1.0 V, a potential below the redox transition from Ni^{2+} ($Ni(OH)_2$) to Ni^{3+} (NiOOH), and at 1.7 V, a potential at which oxygen evolution takes place. The XANES spectra of the preconditioned sample and during the polarization at 1.0 V do not show any differences compared to the initial state. Under OER conditions, the Ni-K edge position remains unchanged as well, although there are clear changes in both the slope and specific features of the spectrum. The spectrum measured at 1.7 V has a lower white line intensity with its maximum shifted to higher energy. It resembles the spectrum of NiOOH, produced by in situ electrochemical oxidation of $Ni(OH)_2$ at 1.6 V_{RHE} and is also similar to the spectra of Ni^{3+} species reported in the literature.[26,27] This change observed under reaction conditions indicates that there was a change in the oxidation state from Ni^{2+} to Ni^{3+} (NiOOH) taking place under OER conditions.[26,27]

The EXAFS spectra measured under operando conditions resemble well those of Ni_xB-300 measured ex situ, revealing the presence of both $Ni(OH)_2$ (peaks at 1.55 and 2.73 Å corresponding to Ni-O and Ni-Ni^{2+} backscattering) and Ni-B in the first coordination sphere, represented by a small peak at 2.15 Å (all uncorrected for phase shift). The fitted Ni-O distance does not change after the electrochemical cycling pretreatment compared to the untreated sample, but reduces, first to 2.05 Å at 1.0 V, and then to 2.03 Å at 1.7 V (see Table S4, Supporting Information). At the same time, the corresponding coordination numbers decrease from 3.7 to 3.3 and 3.0 for the preconditioned sample, and during polarization at 1.0 and 1.7 V, respectively. The Ni-Ni^{2+} coordination number changes drastically from 5.7 to 4.0 when comparing the prepared sample to that measured under operando conditions at 1.7 V. The changes observed in the EXAFS features, associated with the Ni^{2+} state, can have twofold explanation. First, the significant change of coordination number in the Ni-Ni^{2+} backscattering pair compared to Ni-O points to a less ordered structure under harsh OER conditions since the more distant coordination shells are more sensitive to a material's long range order. Another explanation is associated with the chemical state changes observed on the XANES spectra. Both $Ni(OH)_2$ and NiOOH structures form Ni-O as well as Ni-Ni^{X+} ($X = 2, 3$) backscattering signals, however shifted by ≈0.3 Å toward shorter distances in the case of Ni^{3+}. When both structures are present in the sample, the corresponding photoelectron waves interfere destructively due to phase mismatch. This hypothesis is supported by the apparent contraction of the Ni—O bond observed at 1.7 V_{RHE}, consistent with observations by other groups.[7,28]

In the abridged mechanism of O_2 evolution,[29] involving the reaction sequence: (i) $M + OH^- \rightarrow MOH + e^-$; (ii) $MOH + OH^- \rightarrow MO + H_2O + e^-$; (iii) $MO + OH^- \rightarrow MOOH + e^-$; (iv) $MOOH + OH^- \rightarrow MO_2 + H_2O + e^-$; and (v) $MO_2 \rightarrow M + O_2$; Equations (i) to (iii) all involve growth of an oxide layer. In (i) and (ii), Ni

is present as Ni^{2+}, while (iii) involves Ni^{2+} to Ni^{3+} transition, and in (iv) Ni^{3+} is oxidized to Ni^{4+}. Based on this mechanism, a fingerprint of Ni^{4+} should be trackable under active oxygen evolution conditions using a suitable operando technique.[28] By employing pseudo-operando XAFS, and other complementary in situ techniques to track the redox states of Ni and Fe in a Ni-Fe(OOH) catalyst, Strasser and co-workers[28,30] observed that for a low content of Fe in the catalyst, <4%, Ni^{4+} was the dominant redox state of Ni under catalytic OER conditions. Conversely, a high Fe content, >4%, stabilized the Ni^{2+} state thereby suppressing the higher-valent states of Ni (Ni^{3+} and Ni^{4+}) under catalytic O_2 evolution conditions, resulting in faster oxygen evolution kinetics at the expense of the oxidation of Ni^{2+}. The authors concluded based on these observations that $Ni^{2+}Fe^{3+}OOH$ is the active state of the Ni-Fe(OOH) catalyst under catalytic conditions. For bulk electrode materials, the OER takes place on a thin surface oxide-hydroxide layer making it challenging to observe the transient states of OER catalysts whose bulk properties predominate the surface properties by employing an averaging technique. The Ni_xB-300 catalyst probed here comprised of ultrathin sheets of atomic scale thickness (≈6.6 Å), with a core–shell (Ni-B@NiO_x) structure, where the surface properties (Ni^{2+}) predominated the core properties (Ni-B), as demonstrated by XAFS in Figure 3, which makes the catalyst suitable for operando XAFS studies. Our operando XAFS studies did not disclose any features attributable to the Ni^{4+} state at active O_2 evolution potentials. To rationalize this observation on the premise of the mechanism outlined above, deoxygenation of the NiO_2 intermediate, step (v) has to be comparatively faster in relation to the other reaction steps. Interestingly, our observations lead to a conclusion that appears to be coherent with the work of Strasser and co-workers.[28,30] Our findings therefore present new insights into the dynamics of OER catalyst structures under reaction conditions, as well as the dynamics of some transient states of the catalyst during the OER.

3. Conclusion

Nickel boride (Ni_xB) comprised of very thin sheets and small nanoparticles with a Ni-B core and nickel hydroxide shell (Ni-B@$Ni(OH)_2$) structure is unveiled as a highly efficient and stable electrocatalyst for oxygen evolution under alkaline conditions. When supported on nickel foam, the catalyst drives the OER at 20 mA cm^{-2} at only 0.28 V overpotential in 1.0 M KOH. We observed by operando XAFS intactness of the Ni-B core under active oxygen evolution and, simultaneously, a transition of Ni^{2+} to Ni^{3+} (NiOOH) in the shell leading to shortening of Ni—O bonds and increase in disorder of the nickel oxyhydroxide layer. The synthesis of nickel boride is simple and readily scalable, making it a very attractive and competitive nonprecious anode catalyst in ECWS for mass hydrogen production.

Supporting Information

Supporting Information is available from the Wiley Online Library or from the author.

Acknowledgements

The authors are grateful to Mr. Daniel Peters for support with XRD measurements and interpretation, Dr. Wei Xia and Dr. Christoph Somsen for initial TEM analysis and interpretation, Mrs. Sandra Schmidt for scanning electron microscopy (SEM) measurements, and Mr. Martin Trautmann for the AFM measurements. Staff of beamlines 2-2 (Stanford Synchrotron Radiation Lightsource), ID10 (Advanced Photon Source), and SAMBA (SOLEIL) are acknowledged for their support during XAFS measurements. This work was made possible through the financial support from the US National Science Foundation (NSF-Chemistry 1213182) and the Cluster of Excellence RESOLV at RUB (EXC 1069) funded by the Deutsche Forschungsgemeinschaft. B.R.C. and I.S. gratefully acknowledge financial support from the German Federal Ministry of Education and Research (Bundesministerium für Bildung und Forschung, BMBF) under grant No. 03SF0523C, CO2EKAT. MRCAT operations are supported by the Department of Energy and the MRCAT member institutions. This research used resources of the Advanced Photon Source, a U.S. Department of Energy (DOE) Office of Science User Facility operated for the DOE Office of Science by Argonne National Laboratory under Contract No. DE-AC02-06CH11357. Use of the Stanford Synchrotron Radiation Lightsource, SLAC National Accelerator Laboratory, is supported by the U.S. Department of Energy, Office of Science, Office of Basic Energy Sciences under Contract No. DE-AC02-76SF00515. M.d.l.M. and J.A. acknowledge funding from Generalitat de Catalunya 2014 SGR 1638 and the Spanish MINECO coordinated projects between IREC and ICN2 TNT-FUELS and e-TNT and ICN2 Severo Ochoa Excellence Program.

Conflict of Interest

The authors declare no conflict of interest.

Keywords

hydrogen evolution, nickel boride, oxygen evolution, water oxidation, water splitting, XAFS

Received: February 12, 2017
Revised: March 5, 2017
Published online: May 10, 2017

[1] a) F. Barbir, *Solar Energy* **2005**, *78*, 661; b) K. Zeng, D. Zhang, *Prog. Energy Combust.* **2010**, *36*, 307.
[2] C. C. L. McCrory, S. Jung, I. M. Ferrer, S. M. Chatman, J. C. Peters, T. F. Jaramillo, *J. Am. Chem. Soc.* **2015**, *137*, 4347.
[3] T. Reier, M. Oezaslan, P. Strasser, *ACS Catal.* **2012**, *2*, 1765.
[4] Y. Xu, W. Tu, B. Zhang, S. Yin, Y. Huang, M. Kraft, R. Xu, *Adv. Mater.* **2017**, *29*, 1605957.
[5] a) L. J. Enman, M. S. Burke, A. S. Batchellor, S. W. Boettcher, *ACS Catal.* **2016**, *6*, 2416; b) M. S. Burke, M. G. Kast, L. Trotochaud, A. M. Smith, S. W. Boettcher, *J. Am. Chem. Soc.* **2015**, *137*, 3638; c) M. Gong, Y. Li, H. Wang, Y. Liang, J. Z. Wu, J. Zhou, J. Wang, T. Regier, F. Wei, H. Dai, *J. Am. Chem. Soc.* **2013**, *135*, 8452; d) F. Song, X. Hu, *Nat. Commun.* **2014**, *5*, 4477.
[6] X. Lu, C. Zhao, *Nat. Commun.* **2015**, *6*, 6616.
[7] F. Dionigi, P. Strasser, *Adv. Energy Mater.* **2016**, *6*, 1600621.
[8] M. Sun, H. Liu, J. Qu, J. Li, *Adv. Energy Mater.* **2016**, *6*, 1600087.
[9] a) E. J. Popczun, J. R. McKone, C. G. Read, A. J. Biacchi, A. M. Wiltrout, N. S. Lewis, R. E. Schaak, *J. Am. Chem. Soc.* **2013**, *135*, 9267; b) E. J. Popczun, C. G. Read, C. W. Roske, N. S. Lewis, R. E. Schaak, *Angew. Chem., Int. Ed.* **2014**, *53*, 5427; c) X. Long,

G. Li, Z. Wang, H. Zhu, T. Zhang, S. Xiao, W. Guo, S. Yang, *J. Am. Chem. Soc.* **2015**, *137*, 11900; d) W. Zhu, X. Yue, W. Zhang, S. Yu, Y. Zhang, J. Wang, J. Wang, *Chem. Commun.* **2016**, *52*, 1486; e) H. Zhou, F. Yu, Y. Huang, J. Sun, Z. Zhu, R. J. Nielsen, R. He, J. Bao, W. A. Goddard III, S. Chen, Z. Ren, *Nat. Commun.* **2016**, *7*, 12765; f) H. Vrubel, X. Hu, *Angew. Chem., Int. Ed.* **2012**, *124*, 12875.

[10] J. Masa, P. Weide, D. Peeters, I. Sinev, W. Xia, Z. Sun, C. Somsen, M. Muhler, W. Schuhmann, *Adv. Energy Mater.* **2016**, *6*, 1502313.

[11] S. Anantharaj, S. R. Ede, K. Sakthikumar, K. Karthick, S. Mishra, S. Kundu, *ACS Catal.* **2016**, *6*, 8069.

[12] a) S. Zhao, Y. Wang, J. Dong, C.-T. He, H. Yin, P. An, K. Zhao, X. Zhang, C. Gao, L. Zhang, J. Lv, J. Wang, J. Zhang, A. M. Khattak, N. A. Khan, Z. Wei, J. Zhang, S. Liu, H. Zhao, Z. Tang, *Nat. Energy* **2016**, *1*, 16184; b) H. Liang, F. Meng, M. Caban-Acevedo, L. Li, A. Forticaux, L. Xiu, Z. Wang, S. Jin, *Nano Lett.* **2015**, *15*, 1421; c) Z. Lu, H. Wang, D. Kong, K. Yan, P.-C. Hsu, G. Zheng, H. Yao, Z. Liang, X. Sun, Y. Cui, *Nat. Commun.* **2014**, *5*, 4345; d) X. Han, C. Yu, S. Zhou, C. Zhao, H. Huang, J. Yang, Z. Liu, J. Zhao, J. Qiu, *Adv. Energy Mater.* **2017**, *7*, 1602148.

[13] a) G. N. Glavee, K. J. Klabunde, C. M. Sorensen, G. C. Hadjapanayis, *Langmuir* **1992**, *8*, 771; b) P. E. R. Blanchard, A. P. Grosvenor, R. G. Cavell, A. Mar, *Chem. Mater.* **2008**, *20*, 7081.

[14] J. Schreifels, *J. Catal.* **1980**, *65*, 195.

[15] a) S. Carenco, D. Portehault, C. Boissière, N. Mézailles, C. Sanchez, *Chem. Rev.* **2013**, *113*, 7981; b) U. B. Demirci, P. Miele, *Phys. Chem. Chem. Phys.* **2010**, *12*, 14651; c) G. M. Arzac, T. C. Rojas, A. Fernández, *Appl. Catal., B* **2012**, *128*, 39.

[16] J. Suntivich, K. J. May, H. A. Gasteiger, J. B. Goodenough, Y. Shao-Horn, *Science* **2011**, *334*, 1383.

[17] G. P. Shveikin, A. L. Ivanovskii, *Russ. Chem. Rev.* **1994**, *63*, 711.

[18] C. Tang, N. Cheng, Z. Pu, W. Xing, X. Sun, *Angew. Chem., Int. Ed.* **2015**, *54*, 9351.

[19] a) M. Ledendecker, S. Krick Calderón, C. Papp, H.-P. Steinrück, M. Antonietti, M. Shalom, *Angew. Chem., Int. Ed.* **2015**, *54*, 12361; b) L.-A. Stern, L. Feng, F. Song, X. Hu, *Energy Environ. Sci.* **2015**, *8*, 2347; c) M. Shalom, D. Ressnig, X. Yang, G. Clavel, T. P. Fellinger, M. Antonietti, *J. Mater. Chem. A* **2015**, *3*, 8171; d) Y.-P. Zhu, Y.-P. Liu, T.-Z. Ren, Z.-Y. Yuan, *Adv. Funct. Mater.* **2015**, *25*, 7337; e) W. Zhou, X.-J. Wu, X. Cao, X. Huang, C. Tan, J. Tian, H. Liu, J. Wang, H. Zhang, *Energy Environ. Sci.* **2013**, *6*, 2921.

[20] A. Maljusch, O. Conradi, S. Hoch, M. Blug, W. Schuhmann, *Anal. Chem* **2016**, *88*, 7597.

[21] S. Chen, J. Duan, P. Bian, Y. Tang, R. Zheng, S.-Z. Qiao, *Adv. Energy Mater.* **2015**, *5*, 1500936.

[22] H. Liang, A. N. Gandi, D. H. Anjum, X. Wang, U. Schwingenschlogl, H. N. Alshareef, *Nano Lett.* **2016**, *16*, 7718.

[23] B. Zhang, X. Zheng, O. Voznyy, R. Comin, M. Bajdich, M. Garcia-Melchor, L. Han, J. Xu, M. Liu, L. Zheng, F. Pelayo García de Arquer, C. T. Dinh, F. Fan, M. Yuan, E. Yassitepe, N. Chen, T. Regier, P. Liu, Y. Li, P. De Luna, A. Janmohamed, H. L. Xin, H. Yang, A. Vojvodic, E. H. Sargent, *Science* **2016**, *352*, 333.

[24] J. Masa, S. Barwe, C. Andronescu, I. Sinev, A. Ruff, K. Jayaramulu, K. Elumeeva, B. Konkena, B. Roldan Cuenya, W. Schuhmann, *ACS Energy Lett.* **2016**, *1*, 1192.

[25] J. O. Bockris, T. Otagawa, *J. Phys. Chem.* **1983**, *87*, 2960.

[26] S. Gul, J. W. D. Ng, R. Alonso-Mori, J. Kern, D. Sokaras, E. Anzenberg, B. Lassalle-Kaiser, Y. Gorlin, T.-C. Weng, P. H. Zwart, J. Z. Zhang, U. Bergmann, V. K. Yachandra, T. F. Jaramillo, J. Yano, *Phys. Chem. Chem. Phys.* **2015**, *17*, 8901.

[27] A. N. Mansour, *J. Electrochem. Soc.* **1994**, *141*, L69.

[28] M. Gorlin, P. Chernev, J. Ferreira de Araujo, T. Reier, S. Dresp, B. Paul, R. Krahnert, H. Dau, P. Strasser, *J. Am. Chem. Soc.* **2016**, *138*, 5603.

[29] a) Y. Matsumoto, E. Sato, *Mater. Chem. Phys.* **1986**, *14*, 397; b) H. Dau, C. Limberg, T. Reier, M. Risch, S. Roggan, P. Strasser, *ChemCatChem* **2010**, *2*, 724.

[30] J. Ferreira de Araujo, H. Schmies, D. Bernsmeier, S. Dresp, M. Gliech, Z. Jusys, P. Chernev, R. Kraehnert, H. Dau, P. Strasser, *J. Am. Chem. Soc.* **2017**, *139*, 2070.

